

www.acsabm.org Article

Biocompatibility of NbTaTiVZr with Surface Modifications for **Osteoblasts**

Shih-Jie Lin,*, Jia-An Lin, Wei Yu, Chanho Lee, Chun-Yu Hung, Jonathan D Poplawsky, Peter K. Liaw, and Yi-Chia Chou*



Cite This: ACS Appl. Bio Mater. 2022, 5, 642-649

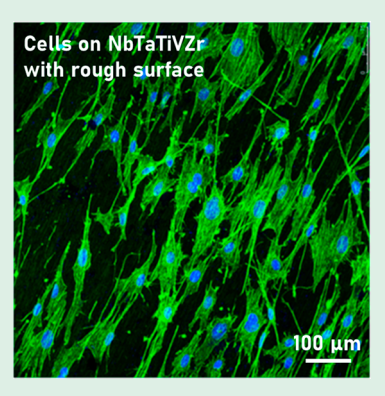


ACCESS |

Metrics & More

Article Recommendations

ABSTRACT: We report a potential biomedical material, NbTaTiVZr, and the impact of surface roughness on the osteoblast culture and later behavior based on in vitro tests of preosteoblasts. Cell activities such as adhesion, viability, and typical protein activity on NbTaTiVZr showed comparable results with that of commercially pure Ti (CP-Ti). In addition, NbTaTiVZr with a smooth surface exhibits better cell adhesion, viability, and typical protein activity which shows that surface modification can improve the biocompatibility of NbTaTiVZr. This supports the biological evidence and shows that NbTaTiVZr can potentially be evaluated as a biomedical material for clinical use.



KEYWORDS: biomedical material, NbTaTiVZr, surface modification, in vitro test, biocompatibility

■ INTRODUCTION

Current biomedical alloys still encounter limitations during clinical applications, 1-3 such as stress shielding, tribo-corrosion failure, and adverse local tissue reactions. Ideal alloys with enhanced mechanical and chemical properties, including a moderate elastic modulus, better wear, and corrosion resistance, have attracted attention as biomedical implants.⁴ The bioalloy design has been widely investigated. Surface modifications, including nanograined, immersion, etching, dealloying, and coating, have been introduced one after another to enhance the degradation resistance and biocompatibility.6-14 A new generation of multicomponent materials, called high-entropy alloys (HEAs), has been developed to meet such demands in the biomedical field. With an approximately equiatomic ratio of multiple elemental components to increase the configurational entropy, the complicated blend of different atomic elements in HEAs could cause the formation of solid solutions, which have an obviously distorted lattice inside and strengthened mechanical properties. 15-18 Because of its nearly equiatomic ratio nature, the constituent elements of HEAs might be decisive in the microstructure and biocompatibility, which makes them new metallic biomaterials (denoted as bio-HEAs).

Formation of a single solid solution 19 could give rise to an obvious lattice distortion, which accordingly strengthens the alloy. In the case of HEAs consisting of only simple single solid-solution phases, the strengthening mechanism is due to the lattice distortion and shear-modulus distortion.²⁰ It is

known that hardness and strength are roughly proportional to each other, so that HEAs with lattice or modulus distortion result in a higher strength and hardness. In bio-HEA applications of hip prosthetic arthroplasty, wear resistance is an important property in biomaterials used in the bearing surface of articulation. Refractory bio-HEAs, such as niobiumtantalum-titanium-vanadium (NbTaTiV), may be considered due to its high hardness at room temperature.²¹ In the previous work, lattice distortion was found to have nonnegligible impacts on the mechanical properties, especially for HEAs.²² This encouraged us to study the biocompatibility of this potential bio-HEA for orthopedic implants.

Ti-based titanium-niobium-zirconium-tantalum (TiNbZr-Ta) alloys have been investigated as superior Ti alloy biomaterials.²³⁻³¹ Moreover, a novel titanium-niobiumzirconium-tantalum-molybdenum (TiNbTaZrMo) bio-HEA was developed from nontoxic constituent elements and showed excellent strength with deformability, excellent corrosion resistance, and superior biocompatibility. 32-36 The constituent elements of TiNbTaZrMo bio-HEAs were mainly

Received: October 22, 2021 Accepted: November 30, 2021 Published: January 26, 2022





MATERIALS AND METHODS

Alloy Fabrication. The nominal chemical composition of the present HEA is Nb₂₀Ta₂₀Ti₂₀V₂₀Zr₂₀ in atomic percentage (atom %). The HEAs were prepared from Nb, Ta, Ti, V, and Zr 99.99 weight percent (wt %) pure elements using the vacuum-arc-melting facility. The melting chamber was initially evacuated to a pressure of 10⁻⁵ Torr. Then, the high-purity argon gas was injected into the chamber to generate a stable arc beam. To achieve a fully homogeneous distribution of elements, the ingot was melted and solidified over 10 times by flipping them over between each repeat. From the prepared ingot alloy, the cylindrical rod samples with a 4 mm diameter and 60 mm length were fabricated using drop casting to conduct the microstructural investigations and compressive mechanical tests. These alloys were sealed into a vacuumed (10⁻² Torr) quartz tube to avoid oxidation and experienced a systematic heat treatment at 1200 °C for 12 h to achieve chemical homogeneity. Then, the samples were water quenched. Disc-shaped samples for compression testing with dimensions of approximately 4 mm in diameter and 2 mm in height were cut from the ingots by a diamond saw.

Surface Finish. The samples were used in in vitro tests to investigate biocompatibility. The surfaces of the samples were mechanically polished using sandpaper and a diamond paste. Prior to in vitro experiments, the samples were sterilized by ethanol and placed individually into a 24-well plate (n=6). Both NbTaTiVZr alloys and commercially pure Ti (CP-Ti) disc-shaped samples were mechanically polished on sandpaper to achieve three different surface finishes from the roughest to the smoothest. Owing to the different hardness between NbTaTiVZr and CP-Ti, different grits of sandpaper were used to create a significant difference in the surface roughness on each material.

- (1) For NbTaTiVZr, SiC sandpaper in a sequence of 400, 600, and 400 grit was used to achieve the roughest surface. The 600-grit sandpaper was employed halfway to ensure that the deepest scratches on the samples were from 400 grit sandpaper. The intermediate one was ground using SiC sandpaper in a sequence of 1200, 2500, and 1200 grit. The 2500-grit sandpaper was used for the same purpose as mentioned above.
- (2) For CP-Ti, SiC sandpaper in a sequence of 600, 1200, and 600 grit was used to achieve the roughest surface. The 1200-grit sandpaper was employed halfway to ensure that the deepest scratches on the samples were from 600 grit sandpaper. The intermediate one was ground using SiC sandpaper in a sequence of 2500, 4000, and 2500 grit. The 4000-grit sandpaper was used for the same purpose as mentioned above.
- (3) As for the smoothest surface finishes, both NbTaTiVZr and CP-Ti were ground employing SiC sandpaper of approximately 600, 1200, 2000, 2500, and 4000 grit followed by polishing with the 1, 0.3, and 0.02 μm aluminum oxide (Al₂O₃) slurry sequence to achieve a mirror-like surface.

All samples were cleaned in acetone, ethanol, and deionized water subsequently and characterized before in vitro experiments.

Composition and Microstructure Analysis. The microstructures of the surfaces of the heat-treated NbTaTiVZr alloys were studied using backscattered-electron (BSE) imaging of scanning electron microscopy (SEM) and neutron diffraction. To observe the atomic-scale elemental distribution to confirm the homogenization of the NbTaTiVZr HEA, the chemical analysis and atomic distribution were determined via atom probe tomography (APT) in laser mode to capture large regions of interest. The acquisition conditions were at a 30 K base temperature, 50 pJ laser energy, and 200 kHz pulse

repetition rate with a detection rate of 0.0005 ions per pulse. Data was collected through a CAMECA local electrode atom probe (LEAP) 4000XHR equipped with an energy-compensated reflection lens and a 10 ps 355 nm ultraviolet (UV) pulsed laser. The acquired data were reconstructed and analyzed using the (IVAS) software (version 3.6.12).³³ SEM was employed by a Zeiss Auriga 40 equipped with Everhart—Thornley secondary electrons (SE) and a BSE detector.

Surface Morphology and Roughness. After obtaining different surface finishes, the surface morphologies of the samples were examined using an OLYMPUS BX51 M optical microscope at 20× magnification. Moreover, the surface roughness was measured using a Veeco DEKTAK 150 Stylus Profiler. The profiler employs a diamond-made probe to traverse the surface of the specimen and thus to acquire the details of the surface profile. When the probe is scanning along a surface, feedback forces from the specimen push up against the probe and spontaneously generate signals recorded by a sensor. In this paper, a total of six random scans from different positions with a scanning distance of 1 mm for each scan were carried out on each specimen. Average and standard deviation values were reported as surface-roughness results.

Surface Free Energy (SFE). The surface free energy (SFE) for the samples was determined through the sessile drop contact angle measured by a contact angle goniometer, a First Ten Angstroms 32 (FTA 32). On the basis of the Owens-Wendt model,³⁴ polar and dispersive interactions are considered in the calculation of the SFE. During the measurements, a 0.5 μ L droplet of polar (deionized water, DI water) and dispersive (diiodomethane, DII) liquids was placed on each specimen. The two specific liquids were chosen to simulate the growth medium of human body fluids comprised of inorganic and organic ingredients. Seven measurements from different positions of each specimen were carried out, and their average and standard deviation values were reported as contact angle results. Contact angle results not only reveal the surface wettability but also serve as required components of the SFE calculation based on the Owens-Wendt model.³⁴ The SFE results reported in the paper were calculated using the Owens-Wendt equation 34

$$1 + \cos \theta = 2(\gamma_s^d)^{1/2} [(\gamma_l^d)^{1/2}/\gamma_l] + 2(\gamma_s^p)^{1/2} [(\gamma_l^p)^{1/2}/\gamma_l]$$
 (1)

where θ is the contact angle, γ_1 is the SFE of the liquid used in the measurements, γ_s is the SFE of the test specimen, and superscripts d and p denote the dispersive and polar components of SFE. The SFE of each specimen can be calculated as

$$\gamma_{\rm s} = \gamma_{\rm s}^{\rm d} + \gamma_{\rm s}^{\rm p} \tag{2}$$

Cell Culture and Cell Seeding. The murine calvarial preosteoblast cell line, MC3T3-E1, has been widely used as a model system in bone biology and represents results from human cells, 35,36 MC3T3-E1 subclone 4 (ATCC) was used in in vitro biochemical tests. Cells were cultured in a Petri dish with a growth medium comprised of a minimum amount of essential medium with alpha modifications (MEM α) supplemented with 10 wt % (wt %) fetal bovine serum (FBS) and 1 wt % antibiotics. The medium was renewed every 2–3 days. After culturing, cells were detached from the Petri dish using trypsin and seeded in a 24-well culture plate on the surface of each specimen. Cells were subsequently incubated in an incubator at 37 °C with 5 wt % $\rm CO_2$ supplied. The incubation time varied in different in vitro tests.

Cell Morphology. Cell morphologies for all samples were imaged using SEM after 4 h of incubation; 1×10^4 cells were seeded on each specimen and incubated for 4 h. Before imaging, the cells were fixed and dried in advance through the steps described below. After 4 h of incubation, the cells were washed with phosphate-buffered saline (PBS) three times followed by primary fixation with 3 wt % glutaraldehyde for 1 h at room temperature (RT). After rinsing the samples with PBS another three times, postfixation was performed with 1 wt % osmium tetroxide for 1 h at RT. Postfixed samples were dehydrated with ascending grades of ethanol (25, 50, 75, 95, and 100 wt %) for 10 min each grade. The dried samples were prepared by a critical point drying method 37 prior to examination by SEM.

ACS Applied Bio Materials www.acsabm.org

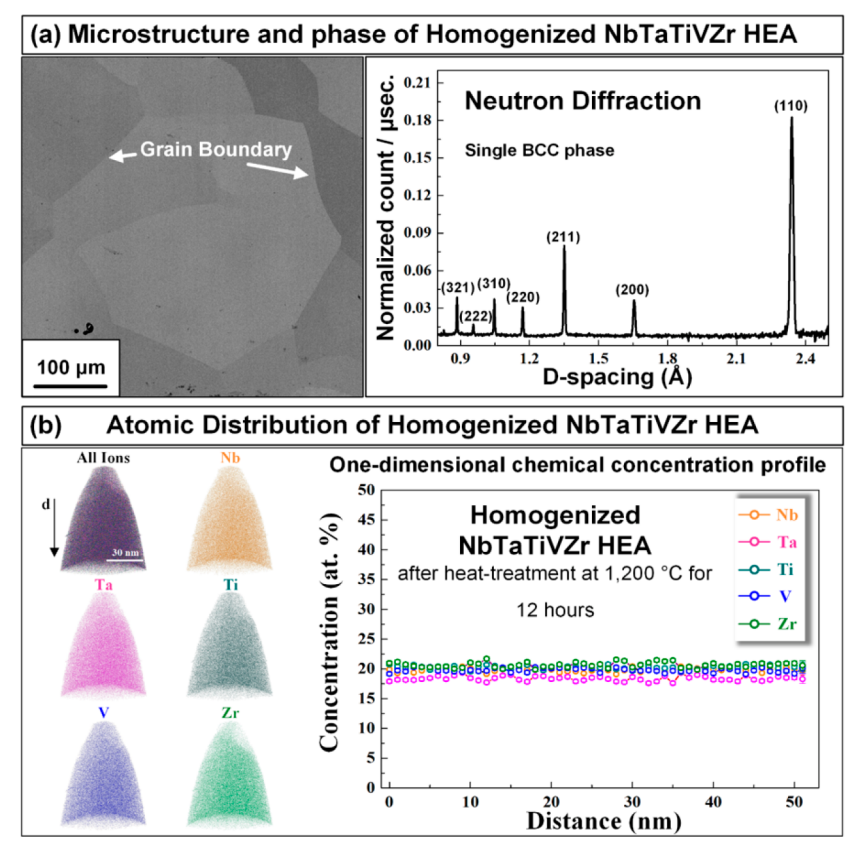


Figure 1. (a) SEM-BSE image and neutron diffraction pattern of the homogenization-treated NbTaTiVZr refractory HEA. (b) Three-dimensional atom maps of individual elements (left), and concentration—depth profile of all alloying elements taken along the 51 nm cylindrical sample via the APT technique.

Actin Cytoskeleton Development. Actin cytoskeleton development was demonstrated with fluorescent imaging after 16 h of incubation; 2.5×10^3 cells were seeded on each specimen and incubated for 16 h. Prior to imaging, actin filaments (F-actin) of the cytoskeleton were labeled by incubating the cells with CytoPainter Phalloidin-iFluor 488 reagent (1:1000 dilution) (Abcam). Cell nuclei were stained with ClonFluor Mounting Medium with 4',6-diamidino2-phenylindole dihydrochloride (DAPI) (Taiclone), which is commonly used in labeling nuclei. All samples were viewed with a fluorescence microscope, Leica TCS SP8 stimulated emission depletion (STED).

Cell Viability. Cell viability was analyzed by a 2,3-bis(2-methoxy4-nitro-5-sulfophenyl)-2H-tetrazolium-5-carboxanilide (XTT)-based cell proliferation kit (Cayman) after 3 and 7 days of incubation due to a large number of cells forming. The XTT assay can detect the average nucleic acid content or metabolic activity in viable cells, which are generally applied in cell growth and differentiation studies; 1×10^3 cells were seeded on each specimen for the 3 day XTT assay, and 5×10^3 cells were seeded for the 7 day XTT assay. After incubation, samples were placed in a well with a culture medium as $50~\mu$ L of activated XTT reagent ($20~\mu$ L of the activation reagent per milliliter of XTT reagent) was added in it and then incubated for 3 h. Gentle shaking was performed after 3 h of incubation in order to distribute the dye in the well. The absorbance of the supernatants was measured against the blank at 450 nm using a spectrophotometer, TECAN Infinite 200 Pro.

Cell Differentiation. Cell differentiation from preosteoblasts to osteoblasts was characterized as the alkaline phosphatase (ALP) activity; 5×10^3 cells were seeded on each specimen. After 7 days of incubation, our growth medium was supplemented with 10^{-7} M dexamethasone (Sigma-Aldrich, USA), 50 μ g mL⁻¹ ascorbic acid (Sigma-Aldrich, USA), and 8 mM β -glycerophosphate (Sigma-Aldrich, USA) to allow cell differentiation for 21 days.

Alkaline Phosphatase Activity (ALP). The ALP activity measurement by Western Blot using an Alkaline Phosphatase Activity Colorimetric Assay Kit (BioVision, USA) was determined by the amount of p-nitrophenol (pNP) produced by hydrolysis of the p-nitrophenyl phosphate (pNPP) in the presence of ALP as a catalyst. It is a common test in clinical settings. During the measurement, cell layers were lysed with 100 μ L of assay buffer. Afterward, 50 μ L of the lysate was added into another 24-well plate, and the total volume was brought to 80 μ L with assay buffer. Then, 50 μ L of pNPP was added to each well and mixed well. After 60 min of incubation at RT and being protected from light, 20 μ L of the stop solution from the kit was added to each well to terminate the reaction. The absorbance was measured at 405 nm.

Statistical Analysis. Cell-culture experiments were all performed simultaneously, and each was repeated at least once. Data is reported as the mean \pm standard error of the mean. Student's t-test and the P-value approach were involved in statistical comparisons. A P value less than 0.05 is considered statistically significant (denoted by asterisks).

■ RESULTS AND DISCUSSION

Microstructural Characterization, Phase Identification, and Atomic Distribution. Figure 1a shows the SEM-BSE image and neutron diffraction pattern of the homogenized NbTaTiVZr HEA. The typical single-phase microstructure was obtained after the homogenization treatment at 1200 °C for 12 h. With the simple microstructure, the neutron diffraction pattern reveals the existence of a single body-centered cubic (BCC) phase with a lattice constant of 3.3092 Å. The atomic-scale elemental distribution for the present HEA was confirmed by the APT technique, as illustrated in Figure 1b. The three-dimensional (3D) atom maps for each of composed elements show the homogeneous atomic distribution of

Article

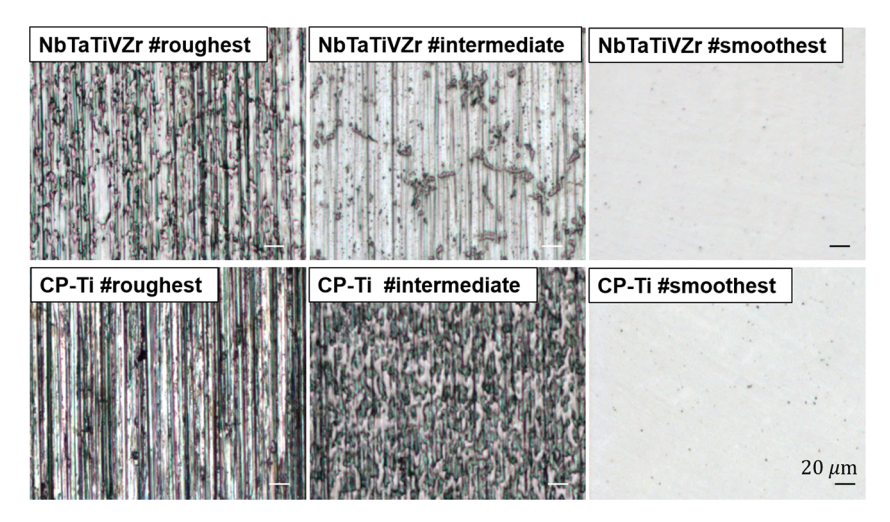


Figure 2. Optical microscopic images of the surface textures of NbTaTiVZr and CP-Ti samples after surface treatments.

alloying elements without any chemical segregation. The chemical homogeneity for NbTaTiVZr HEA was quantitatively verified by a one-dimensional chemical concentration profile, as shown on the right side of Figure 1b. Consistent with the results of the 3D atom maps, there is no statistically considerable concentration fluctuation, indicating a random elemental distribution in the single BCC solid—solution phase. The measured averages of atomic fraction for Nb, Ta, Ti, V, and Zr are 19772, 18 100, 20 267, 19993, and 20 683 atom percent, respectively, showing that each element was distributed as a nearly equiatomic percentage throughout the 51 nm cylindrical sample.

Surface Morphology and Roughness. The surface morphologies of the NbTaTiVZr and CP-Ti samples after surface-roughing treatments were inspected with an optical microscope (OM), as shown in Figure 2. The surface of each sample was intentionally scratched along the same direction, creating oriented grooves with different depths for later cell experiments. The width and roughness using different orders of sandpaper grinding correspond with the sandpaper grits where the widest grooves were generated by the lowest orders of sandpapers and those from the higher orders of sandpapers were narrower. The depth of the two samples could be roughly compared by the contrast of the OM images. The polished samples display nearly mirror-like surfaces. Note that inconspicuous grooves found on the polished surfaces, which might be generated during mechanical polishing, were much less visible than those from the other two conditions of treatments. Hence, the effects of surface conditions from later cell experiments could provide reasonable comparisons.

The surface roughness values of those samples were measured and are listed in Table 1. The values were higher (the surface was rougher) when the grits of the used sandpapers were lower in both NbTaTiVZr and CP-Ti. The

Table 1. Values of Surface Roughness after Surface Treatments^a

	CP-Ti		
600 grit	0.113 ± 0.0197	0.310 ± 0.0671	
1200 grit	0.086 ± 0.0015	0.102 ± 0.0179	
polished	0.028 ± 0.0045	0.028 ± 0.0050	

 $^{^{}a}n = 5$. Units: micrometers.

quantitative roughness was confirmed. The two types of materials with intermediate and smoothest surface finishes led to nearly identical roughness. However, since NbTaTiVZr possesses a much higher hardness than CP-Ti does, it was difficult for us to leave wide and deep grooves on NbTaTiVZr. Therefore, the difference between the two types of the roughest samples were significant. Nevertheless, we compared the cell behaviors on the types of materials and surface roughness separately. Note that the roughness measured on the specimens is below 0.5 μ m, so the impact that roughness has on the contact angle is thought to be insignificant.

SFE. The SFE was determined by the dispersive and polar contact angle measurements of different alloy samples before in vitro tests. The SFE results before in vitro experiments are shown in Table 2. The SFE values were comparable in both materials. This trend may indicate that NbTaTiVZr may have a comparable biocompatibility with CP-Ti since the SFE value of the specimens may imply the chance for cells to attach, achieving a reduction of the Gibbs free energy. Subsequent in vitro tests were carried out to provide evidence for our prediction.

Cell Morphology. The cell morphology after 4 h of incubation on the specimens was examined by SEM (Figure 3). The SEM images, in which specimens were covered with cells, suggested that most cells were initially well fixed or highly adhered on all of the specimen surfaces.

Actin Cytoskeleton Development. The cell morphology of the adhered cells after 16 h of incubation was shown in the fluorescence images (Figure 4). As the actin cytoskeleton is responsible for the cell-structure support, alteration in shape, and cell migration, the shape and distribution of the cells and actin filament (F-actin) arrangement were studied. After 16 h of incubation, the cells developed the actin cytoskeleton (green) and dendritic filopodia. On the roughest surfaces, the cells were mostly presented in an elongated slender shape and extended along the grooves. With the surface being smoother, more polygonal cells were observed. On the smoothest surfaces, the cells were not aligned in a specific direction due to no grooves to attach on or anchor to. Figure 4 shows cells after 16 h of incubation where cells were mostly present in an elongated slender shape and extended along the grooves on rough surfaces. We presumed that the grooves on a rough surface act as high-energy sites for cells to easily attach on, achieving a reduction of the Gibbs free energy.

Table 2. SFE Results for Samples before In Vitro Tests^a

	$\gamma_{ m s}^{ m d}$		$\gamma_{ m s}^{ m p}$		$\gamma_{ m s}$				
	NbTaTiVZr	CP-Ti	NbTaTiVZr	CP-Ti	NbTaTiVZr	CP-Ti			
roughest	32.35 ± 0.45	24.59 ± 0.99	2.69 ± 0.36	0.84 ± 0.22	35.04 ± 0.43	25.42 ± 0.85			
intermediate	33.38 ± 0.78	36.08 ± 0.50	1.69 ± 0.36	4.24 ± 0.44	35.07 ± 0.98	40.31 ± 0.57			
smoothest	33.18 ± 1.11	35.90 ± 1.37	4.62 ± 0.60	0.97 ± 0.17	37.79 ± 0.81	36.87 ± 1.29			
$^{a}n = 5$. γ_{s}^{p} , polar part of SFE; γ_{s}^{d} , dispersive part of SFE; γ_{s} SFE.									

NbTaTiVZr #intermediate

NbTaTiVZr #smoothest

100 μm

CP-Ti #roughest

CP-Ti #intermediate

CP-Ti #smoothest

Figure 3. SEM images showing MC3T3-E1 cell morphology after 4 h of incubation on specimens.

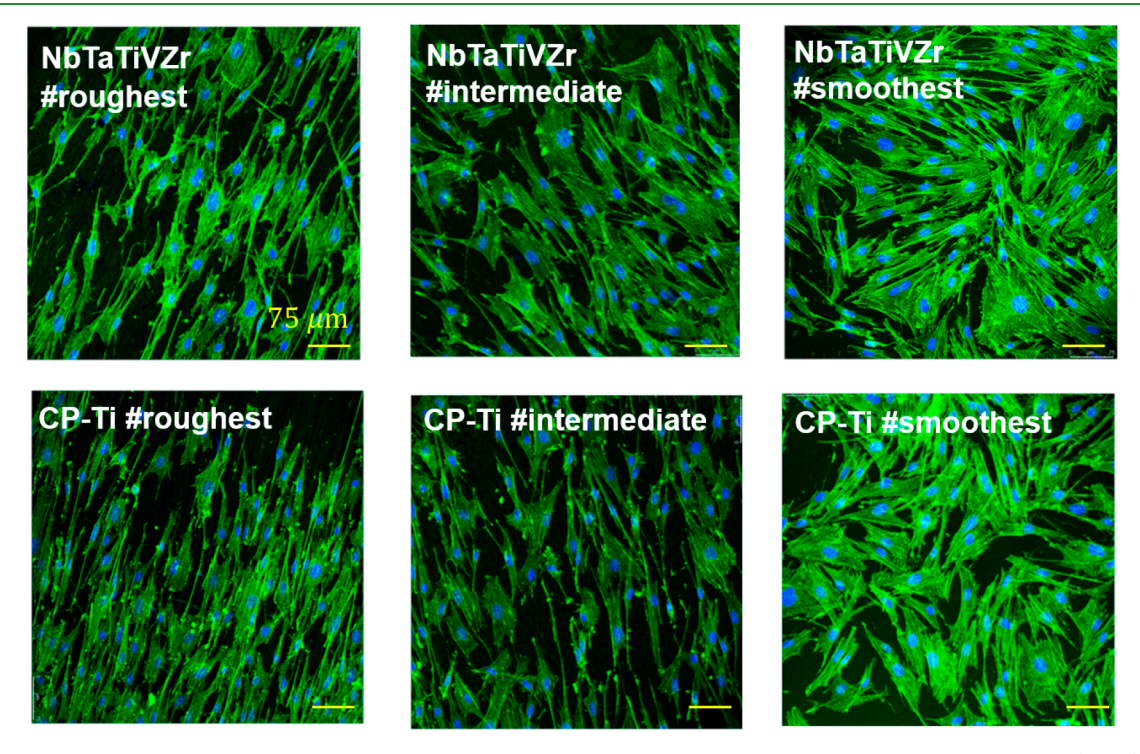
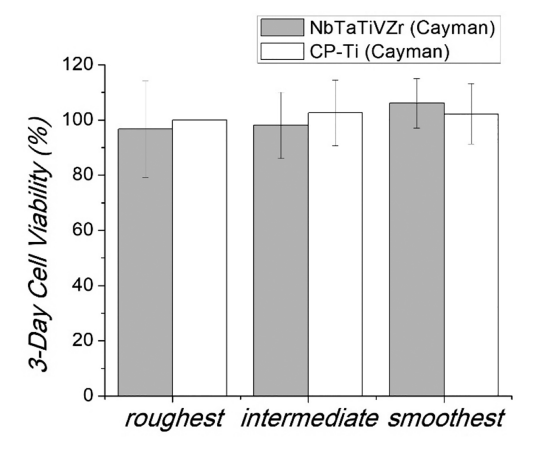


Figure 4. Fluorescence images for MC3T3-E1 cells adhered on the samples after 16 h of incubation, showing the cytoskeleton (green) and nuclei (blue). Phalloidin (green) stains actin filaments (F-actin), and DAPI (blue) stains nuclei.

Cell Viability. A histogram of the XTT assay results (Figure 5) shows the cell viability after 3 and 7 days of incubation, and CP-Ti #600 was set as the benchmark (100%) for easy comparison. A significant increasing trend was found in NbTaTiVZr, while the roughness effect was trivial in CP-Ti in the first 3 days. However, the cell viability after 7 days was not affected by roughness, possibly because the specimen

surfaces were covered by cells and thus reduce the roughness effect. In general, NbTaTiVZr had a comparable biocompatibility with CP-Ti, which was coherent with our prediction based on comparable SFE values. Moreover, NbTaTiVZr exhibited a general higher level in the XTT activity as its surface became smoother and was superior to CP-Ti for the 7 day XTT assay. This feature not only showed that it may be

ACS Applied Bio Materials www.acsabm.org Article



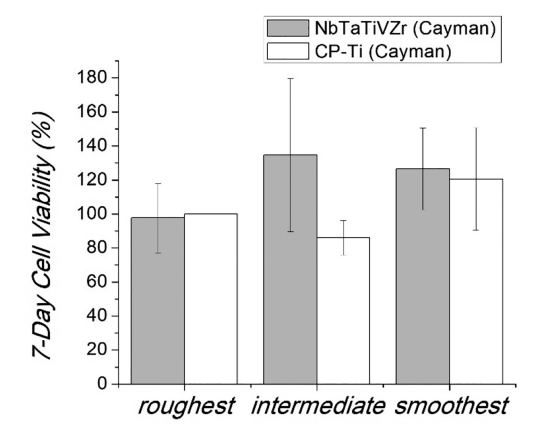


Figure 5. XTT assay results representing viability of MC3T3-E1 cells after 3 and 7 days of incubation. Results are presented as percentage of that on the samples (n = 3, *P < 0.05). P value less than 0.05 is considered statistically significant (denoted by asterisks).

feasible to improve the biocompatibility of NbTaTiVZr by polishing but also implied that NbTaTiVZr may become a potential biomedical material in the near future.

Cell Differentiation. In order to monitor cell maturation from preosteoblast MC3T3-E1 cells to osteoblasts, the alkaline phosphatase (ALP) activity was examined as it is one of the typical proteins released during cell differentiation. The ALP activities (Figure 6) after 7 days of growth and 21 days of differentiation were normalized to the total protein content, and CP-Ti #600 was set as the benchmark (100%) for easy comparison. The results showed that the ALP activity on NbTaTiVZr has a dependence on the surface roughness, where the typical protein activity increased as the surface became smoother. Although an overall superior ALP activity was shown on CP-Ti and was also less affected by the surface roughness, NbTaTiVZr still was competitive when complete polishing was achieved.

CONCLUSIONS

In summary, we reported a potential biomedical material, NbTaTiVZr, and the impact of surface roughness based on in vitro tests of preosteoblasts. Cell activities, such as adhesion, viability, and typical protein activity on NbTaTiVZr, showed comparable results with that of CP-Ti, which was coherent with the prediction based on comparable SFE values. Moreover, a slight increase in biocompatibility can be found

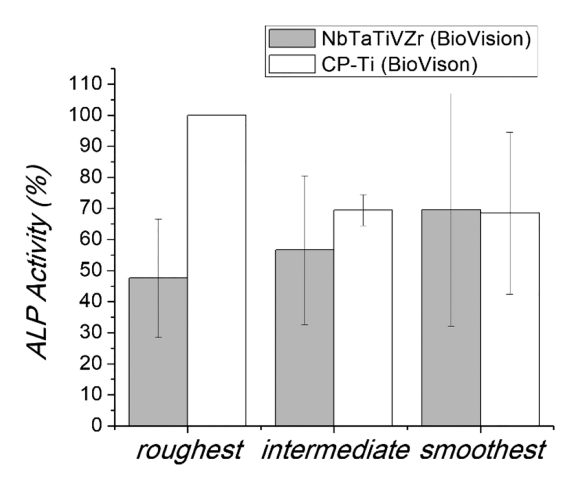


Figure 6. Normalized ALP activities of MC3T3-E1 cell lysates after 7 days of growth and 21 days of differentiation. Results are presented as the percentage of that on the samples (n = 3, *P < 0.05). P value less than 0.05 is considered statistically significant (denoted by asterisks).

in NbTaTiVZr as the surface became smoother. These results show a way of improving the biocompatibility of NbTaTiVZr and also propose a potential biomedical material with biological evidence.

AUTHOR INFORMATION

Corresponding Authors

Shih-Jie Lin — Department of Orthopaedic Surgery, New Taipei Municipal TuCheng Hospital, Chang Gung Memorial Hospital, New Taipei City 23653, Taiwan; Bone and Joint Research Center, Chang Gung Memorial Hospital, Linkou 33305, Taiwan; Department of Chemical Engineering, National Tsing Hua University, Hsinchu 30010, Taiwan; Email: b9002092@cgmh.org.tw

Yi-Chia Chou — Department of Electrophysics, National Yang Ming Chiao Tung University, Hsinchu 30010, Taiwan; Department of Materials Science and Engineering, National Taiwan University, Taipei 10617, Taiwan; orcid.org/0000-0002-7775-2927; Email: ycchou@ntu.edu.tw

Authors

Jia-An Lin – Department of Electrophysics, National Yang Ming Chiao Tung University, Hsinchu 30010, Taiwan Wei Yu – Department of Electrophysics, National Yang Ming Chiao Tung University, Hsinchu 30010, Taiwan

Chanho Lee — Department of Materials Science and Engineering, The University of Tennessee, Knoxville, Tennessee 37996-2100, United States; Materials Science and Technology Division, Los Alamos National Laboratory, Los Alamos, New Mexico 87545, United States

Chun-Yu Hung – Department of Orthopaedic Surgery, Chang Gung Memorial Hospital, Yunlin 63863, Taiwan

Jonathan D Poplawsky — Center for Nanophases Materials Sciences, Oak Ridge National Laboratory, Oak Ridge, Tennessee 37831, United States; ⊙ orcid.org/0000-0002-4272-7043

Peter K. Liaw – Department of Materials Science and Engineering, The University of Tennessee, Knoxville, Tennessee 37996-2100, United States

Complete contact information is available at: https://pubs.acs.org/10.1021/acsabm.1c01103

Author Contributions

[⊥]S.-J.L. and J.-A.L.: These authors contributed equally **Notes**

The authors declare no competing financial interest.

ACKNOWLEDGMENTS

We acknowledge funding from the Ministry of Science and Technology of Taiwan under Grant No. MOST-110-2636-M-009-008 (Young Scholar Fellowship Program) and Chang Gung Medical Foundation under Grant No. CMRPG3J1131 and CMRPVVK0141 (Biomedical Application Research of Novel High Entropy Alloy NbTaTiVZr). We also acknowledge the core facility support in National Yang Ming Chiao Tung University (NYCU) from MOST. The present work was partially supported by the "High-Entropy Materials Center" from The Featured Areas Research Center Program within the framework of the Higher Education Sprout Project by the Ministry of Education (MOE) in Taiwan. C.H.L. and P.K.L. very much appreciate supports from the National Science Foundation (DMR-1611180 and 1809640) with program directors Drs. J. Yang, G. Shiflet, and D. Farkas and the US Army Research Office (W911NF-13-1-0438 and W911NF-19-2-0049) with program managers Drs. M. P. Bakas, S. N. Mathaudhu, and D. M. Stepp. APT was conducted at ORNL's Center for Nanophase Materials Sciences (CNMS), which is a U.S. DOE Office of Science User Facility with proposal number CNMS2015-312 and run number R29-13561.

REFERENCES

- (1) Wise, D. L.; Altobelli, D. E.; Gresser, J. D.; Trantolo, D. J.; Yaszemski, M. J. *Human biomaterials applications*; Humana Press: Totowa, NJ, 2010.
- (2) Ratner, B. D. Biomaterials science: an introduction to materials in medicine; Elsevier/Academic Press: Amsterdam; Boston, MA, 2013.
- (3) Yaszemski, M. J.; Trantolo, D. J.; Lewandrowski, K.-U.; Hasirci, V.; Altobelli, D. E.; Wise, D. L. *Biomaterials in orthopedics*; Marcel Dekker: New York, 2004.
- (4) Navarro, M.; Michiardi, A.; Castano, O.; Planell, J. A. Biomaterials in orthopaedics. *J. R. Soc., Interface* **2008**, 5 (27), 1137–58.
- (5) Li, H.; He, W.; Pang, S.; Liaw, P. K.; Zhang, T. In vitro responses of bone-forming MC3T3-E1 pre-osteoblasts to biodegradable Mg-based bulk metallic glasses. *Mater. Sci. Eng., C* **2016**, *68*, *632*–*641*.
- (6) Huang, L.; Cao, Z.; Meyer, H. M.; Liaw, P. K.; Garlea, E.; Dunlap, J. R.; Zhang, T.; He, W. Responses of bone-forming cells on pre-immersed Zr-based bulk metallic glasses: Effects of composition and roughness. *Acta Biomater.* **2011**, *7* (1), 395–405.
- (7) Ion, R.; Mazare, A.; Dumitriu, C.; Pirvu, C.; Schmuki, P.; Cimpean, A. Nanochannelar Topography Positively Modulates Osteoblast Differentiation and Inhibits Osteoclastogenesis. *Coatings* **2018**, *8* (9), 294.
- (8) Wu, S.; Weng, Z.; Liu, X.; Yeung, K. W. K.; Chu, P. K. Functionalized TiO2Based Nanomaterials for Biomedical Applications. *Adv. Funct. Mater.* **2014**, *24* (35), 5464–5481.
- (9) In Nanobiomaterials in hard tissue engineering: applications of nanobiomaterials; Grumezescu, A. M., Ed.; Elsevier, 2016.
- (10) Wang, L.; Zhou, W.; Yu, Z.; Yu, S.; Zhou, L.; Cao, Y.; Dargusch, M.; Wang, G. An In Vitro Evaluation of the Hierarchical Micro/Nanoporous Structure of a Ti3Zr2Sn3Mo25Nb Alloy after Surface Dealloying. ACS Appl. Mater. Interfaces 2021, 13 (13), 15017–15030.
- (11) Rahman, M. M.; Balu, R.; Abraham, A.; Dutta, N. K.; Choudhury, N. R. Engineering a Bioactive Hybrid Coating for In Vitro Corrosion Control of Magnesium and Its Alloy. *ACS Applied Bio Materials* **2021**, *4* (7), 5542–5555.

- (12) Wang, T.; Huang, L.; Liu, Y.; Li, X.; Liu, C.; Handschuh-Wang, S.; Xu, Y.; Zhao, Y.; Tang, Y. Robust Biomimetic Hierarchical Diamond Architecture with a Self-Cleaning, Antibacterial, and Antibiofouling Surface. ACS Appl. Mater. Interfaces 2020, 12 (21), 24432–24441.
- (13) Luo, J.; Zhou, Q.; Hu, X.; Hou, X.; Li, D.; Guo, S.; Sun, S. Magnetic Field-Guided MoS2/WS2 Heterolayered Nanofilm Regulates Cell Behavior and Gene Expression. *ACS Applied Nano Materials* **2021**, *4* (10), 10828–10835.
- (14) Handschuh-Wang, S.; Wang, T.; Tang, Y. Ultrathin Diamond Nanofilms—Development, Challenges, and Applications. *Small* **2021**, 17 (30), 2007529.
- (15) Cantor, B.; Chang, I. T. H.; Knight, P.; Vincent, A. J. B. Microstructural development in equiatomic multicomponent alloys. *Mater. Sci. Eng., A* **2004**, 375–377, 213–218.
- (16) Yeh, J. W.; Chen, S. K.; Lin, S. J.; Gan, J. Y.; Chin, T. S.; Shun, T. T.; Tsau, C. H.; Chang, S. Y. Nanostructured high-entropy alloys with multiple principal elements: Novel alloy design concepts and outcomes. *Adv. Eng. Mater.* **2004**, *6* (5), 299–303.
- (17) Gao, M. C.; Yeh, J.-W.; Liaw, P. K.; Zhang, Y. High-Entropy Alloys Fundamentals and Applications; Springer International Publishing, A.G., 2018.
- (18) Zhang, Y.; Zuo, T. T.; Tang, Z.; Gao, M. C.; Dahmen, K. A.; Liaw, P. K.; Lu, Z. P. Microstructures and properties of high-entropy alloys. *Prog. Mater. Sci.* **2014**, *61*, 1–93.
- (19) Zhang, Y.; Zhou, Y.; Lin, J.; Chen, G.; Liaw, P. Solid-Solution Phase Formation Rules for Multi-component Alloys. *Adv. Eng. Mater.* **2008**, *10*, 534–538.
- (20) Wang, Z.; Fang, Q. H.; Li, J.; Liu, B.; Liu, Y. Effect of lattice distortion on solid solution strengthening of BCC high-entropy alloys. *J. Mater. Sci. Technol.* **2018**, *34* (2), 349–354.
- (21) Guo, W.; Liu, B.; Liu, Y.; Li, T.; Fu, A.; Fang, Q.; Nie, Y. Microstructures and mechanical properties of ductile NbTaTiV refractory high entropy alloy prepared by powder metallurgy. *J. Alloys Compd.* **2019**, 776, 428–436.
- (22) Lee, C.; Song, G.; Gao, M. C.; Feng, R.; Chen, P.; Brechtl, J.; Chen, Y.; An, K.; Guo, W.; Poplawsky, J. D.; Li, S.; Samaei, A. T.; Chen, W.; Hu, A.; Choo, H.; Liaw, P. K. Lattice distortion in a strong and ductile refractory high-entropy alloy. *Acta Mater.* **2018**, *160*, 158–172.
- (23) Geetha, M.; Singh, A. K.; Asokamani, R.; Gogia, A. K. Ti based biomaterials, the ultimate choice for orthopaedic implants A review. *Prog. Mater. Sci.* **2009**, *54* (3), 397–425.
- (24) Niinomi, M. Mechanical biocompatibilities of titanium alloys for biomedical applications. *J. Mech Behav Biomed Mater.* **2008**, *1* (1), 30–42.
- (25) Yuan, Y.; Wu, Y.; Yang, Z.; Liang, X.; Lei, Z.; Huang, H.; Wang, H.; Liu, X.; An, K.; Wu, W.; Lu, Z. Formation, structure and properties of biocompatible TiZrHfNbTa high-entropy alloys. *Mater. Res. Lett.* **2019**, 7 (6), 225–231.
- (26) Senkov, O.; Scott, J.; Senkova, S.; Miracle, D.; Woodward, C. Microstructure and Room Temperature Properties of a High-Entropy TaNbHfZrTi Alloy (Preprint). *J. Alloys Compd.* **2011**, *509*, 6043–8.
- (27) Akahori, T.; Niinomi, M.; Nakai, M.; Nishimura, H.; Takei, Y.; Fukui, H.; Ogawa, M. Wear and Mechanical Properties, and Cell Viability of Gas-Nitrided Beta-Type Ti-Nb-Ta-Zr System Alloy for Biomedical Applications. *Mater. Trans.* **2008**, *49* (1), 166–174.
- (28) Niinomi, M.; Akahori, T.; Nakamura, S.-i.; Fukui, H.; Suzuki, A. Wear Characteristics of Surface Oxidation Treated New Biomedical β -type Titanium Alloy in Simulated Body Environment. *Tetsu to Hagane* **2002**, *88* (9), 567–574.
- (29) Niinomi, M. Biologically and Mechanically Biocompatible Titanium Alloys. *Mater. Trans.* **2008**, 49, 2170–2178.
- (30) Hao, Y. L.; Yang, R.; Niinomi, M.; Kuroda, D.; Zhou, Y. L.; Fukunaga, K.; Suzuki, A. Aging response of the young's modulus and mechanical properties of Ti-29Nb-13Ta-4.6Zr for biomedical applications. *Metall. Mater. Trans. A* **2003**, 34 (4), 1007–1012.

- (31) Niinomi, M.; Nakai, M. Titanium-Based Biomaterials for Preventing Stress Shielding between Implant Devices and Bone. *Int. J. Biomater.* **2011**, 2011, 836587.
- (32) Todai, M.; Nagase, T.; Hori, T.; Matsugaki, A.; Sekita, A.; Nakano, T. Novel TiNbTaZrMo high-entropy alloys for metallic biomaterials. *Scr. Mater.* **2017**, *129*, 65–68.
- (33) Wang, S. P.; Xu, J. TiZrNbTaMo high-entropy alloy designed for orthopedic implants: As-cast microstructure and mechanical properties. *Mater. Sci. Eng., C* **2017**, *73*, 80–89.
- (34) Hori, T.; Nagase, T.; Todai, M.; Matsugaki, A.; Nakano, T. Development of non-equiatomic Ti-Nb-Ta-Zr-Mo high-entropy alloys for metallic biomaterials. *Scr. Mater.* **2019**, *172*, 83–87.
- (35) Yang, W.; Liu, Y.; Pang, S.; Liaw, P. K.; Zhang, T. Bio-corrosion behavior and in vitro biocompatibility of equimolar TiZrHfNbTa high-entropy alloy. *Intermetallics* **2020**, *124*, 106845.
- (36) Ching, W.-Y.; San, S.; Brechtl, J.; Sakidja, R.; Zhang, M.; Liaw, P. K. Fundamental electronic structure and multiatomic bonding in 13 biocompatible high-entropy alloys. *npj Computational Materials* **2020**, *6* (1), 45.
- (37) Rudawska, A.; Jacniacka, E. Analysis for determining surface free energy uncertainty by the Owen-Wendt method. *Int. J. Adhes. Adhes.* **2009**, 29 (4), 451–457.

☐ Recommended by ACS

Comparison of the Microstructure and Biocorrosion Properties of Additively Manufactured and Conventionally Fabricated near β Ti-25Nb-3Zr-3Mo...

Matthew S. Dargusch, Zhiming Shi, et al.

OCTOBER 03, 2019

ACS BIOMATERIALS SCIENCE & ENGINEERING

READ 🗹

Microstructural Evolution, Mechanical Properties, and Preosteoblast Cell Response of a Post-Processing-Treated TNT5Zr β Ti Alloy Manufactured via Selectiv...

Weihuan Kong, Moataz M. Attallah, et al.

MAY 10, 2022

ACS BIOMATERIALS SCIENCE & ENGINEERING

READ 🗹

Li-Doped Ti Surface for the Improvement of Osteointegration

Longhai Qiu, Mei Li, et al.

APRIL 03, 2022 ACS OMEGA

READ Z

Study of Bone Regeneration and Osteointegration Effect of a Novel Selective Laser-Melted Titanium-Tantalum-Niobium-Zirconium Alloy Scaffold

Yu Guo, Yongqiang Hao, et al.

NOVEMBER 04, 2019

ACS BIOMATERIALS SCIENCE & ENGINEERING

READ 🗹

Get More Suggestions >